Naval Research Laboratory
Washington, DC 20375-5320

NRL/6003/MR—2023/1

Comparing 3D Lidar Geometry to Vetted Urban Geometry via CT-Analyst®

JAY BORIS

Chief Scientist
Material Science and Component Technology Directorate

ADAM J. MOSES

KEITH S. OBENSCHAIN

Laboratory for Advanced Computational Physics
Laboratories for Computational Physics and Fluid Dynamics

KIRAN M. DONNELLY

SEAP Summer Intern Program
McLean, VA

GOPAL PATNAIK

Syntek Technologies
Severna Park, MD

January 26, 2023

REPORT DOCUMENTATION PAGE

Form Approved
OMB No. 0704-0188

1. REPORT DATE *(DD-MM-YYYY)*	**2. REPORT TYPE**	**3. DATES COVERED** *(From - To)*
26-01-2023	NRL Memorandum Report	06-30-2022 – 12/20/2022

4. TITLE AND SUBTITLE

Comparing 3D Lidar Geometry to Vetted Urban Geometry via CT-Analyst®

5a. CONTRACT NUMBER

5b. GRANT NUMBER

5c. PROGRAM ELEMENT NUMBER

6. AUTHOR(S)

Jay Boris, PA, Adam J. Moses, Keith S. Obenschain, Kiran M. Donnelly*, and Gopal Patnaik**

5d. PROJECT NUMBER

5e. TASK NUMBER
ERP NWA 100001926918

5f. WORK UNIT NUMBER
1V28

7. PERFORMING ORGANIZATION NAME(S) AND ADDRESS(ES)

Naval Research Laboratory
4555 Overlook Avenue, SW
Washington, DC 20375-5320

8. PERFORMING ORGANIZATION REPORT NUMBER

NRL/6003/MR--2023/1

9. SPONSORING / MONITORING AGENCY NAME(S) AND ADDRESS(ES)

Naval Research Laboratory
4555 Overlook Avenue, SW
Washington, DC 20375-5320

10. SPONSOR / MONITOR'S ACRONYM(S)

11. SPONSOR / MONITOR'S REPORT NUMBER(S)

12. DISTRIBUTION / AVAILABILITY STATEMENT

DISTRIBUTION STATEMENT A: Approved for public release; distribution is unlimited.

13. SUPPLEMENTARY NOTES

*SEAP Summer Intern Program, 714 Ridge Drive, McLean VA 22101; **Syntek Technologies, 845 Baltimore Annapolis Blvd, Severna Park, MD 21146
This is the first NRL Memorandum Report in a series, denoted CTA #1. There will be three. The second and third (CTA #2 and CTA #3) are being assembled now, extensions of this planned NRL memorandum report.

14. ABSTRACT

Airborne lidar measurements of a 3D urban region provide a digital geometry database of 3D buildings and urban terrain that is within a few percent of a vetted geometry database painstakingly assembled from satellite or aircraft stereo imagery. The pacing item in preparing CT-Analyst® contaminant transport software for real time use in a new urban region has been the labor-intensive weeks to months needed to assemble the 1-meter resolution 3D geometry used to precompute the building influences on urban wind fields. The assembly of a good geometry database from lidar now can take only a day or two.

NRL CT-Analyst force-protection software predicts the transport and dispersion of airborne contaminants over complicated-geometry landscapes. This fast (milliseconds) laptop system is also accurate because it is based on 18 wind field maps called NomografsTM that are precalculated for a built-up region. A set of nomografs typically covers a 12 km by 12 km urban region at 5-meter resolution. These nomografs are derived from 3D Computational Fluid Dynamics simulations taking a couple of days on a modest high-performance parallel cluster. This report compares the CT-Analyst contaminant 'density' predictions, using 2-meter resolution nomografs, for a 4 km by 4 km area of downtown Denver based on an existing 'vetted' 3D geometry and the corresponding geometry derived from airborne lidar measurements. The IDA Measure of Effectiveness (MoE), a cloud-to-cloud comparison metric computed at specific times, is used to compare predictions based on the two different geometry datasets. This report shows that lidar-based geometry allows good quality CT-Analyst predictions with much less investment in labor and preparation lead time.

15. SUBJECT TERMS

Computational fluid dynamics Contaminant transport and dispersion through urban geometry
Metrics for comparing different predictions of contaminant clouds

16. SECURITY CLASSIFICATION OF:			**17. LIMITATION OF ABSTRACT**	**18. NUMBER OF PAGES**	**19a. NAME OF RESPONSIBLE PERSON**
					Jay Boris
a. REPORT	**b. ABSTRACT**	**c. THIS PAGE**	U	20	**19b. TELEPHONE NUMBER** *(include area code)*
U	U	U			(202) 767-3055

Standard Form 298 (Rev. 8-98)
Prescribed by ANSI Std. Z39.18

This page intentionally left blank.

1. Introduction and Background:

Software tools to compute the transport of airborne contaminants in cities are based on various modelling approaches. One of these, designed to meet rapid response requirements with higher accuracy, has yielded a portable laptop system for near instantaneous transport and dispersion prediction. This approach, CT-Analyst®, was developed through a collaboration between developers and users in Washington DC and in Hamburg, Germany (Boris, et al, 2010; Leitl, et al, 2016, 2017; Patnaik, et al, 2017). CT-Analyst is reliable, user friendly, and makes very fast prediction of hazardous agent dispersion in complex-geometry areas. CT-Analyst has proved useful in time critical operational situations during detection, alert, and response phases.

CT-Analyst: A computational result is generally more accurate when the model includes more detailed physics but this usually makes it run slower. To solve this speed-vs-accuracy dilemma, we execute 18 large, time-dependent, 3D Computational Fluid Dynamics (CFD) city-wide simulations well in advance, saving out highly compressed wind field databases that incorporate the varying urban airflow over and around the buildings. These simulations treat 18 prevailing wind directions spaced every 20 degrees around the compass that give enough information for all source locations. These wind field databases are called dispersion Nomografs™ and power CT-Analyst on portable computers. Thus FAST3D-CT, the Naval Research Laboratory's (NRL) 3D urban CFD model, underpins the computation of these dispersion nomografs but must be run on a high performance computer system for every urban domain being considered. The one-time computational expense of the nomografs for a new region, is hidden from the users and moved to a one-time preprocessing stage by experts in the laboratory.

The CT-Analyst (Contaminant Transport Analyst) software has been used to provide the ongoing analyses for recent deployments during major events in the Washington DC and Los Angeles areas and for a potentially dangerous toxic release in Hamburg. CT-Analyst provides predictions of an expanding cloud from a short-duration contaminant release or from a continuous plume arising from a steady source such as an industrial leak. The table driven basis of CT-Analyst makes new capabilities possible (Obenschain, et al, 2004; Boris, et al, 2019). These include sensor placement optimization and sensor fusion 'backtrack' to compute unknown source locations. The model accepts qualitative input without requiring knowing a source type or amount. Thus, both sensor input and verbal reports can provide current information regarding the localized presence or absence of contaminants, their concentrations and the local winds.

CT-Analyst's underlying prediction of the contaminant cloud density over an urban region is a snapshot at one specified time that takes a few milliseconds to compute. In this report the wind speed is chosen as 4.0 meters-per-second (mps), a speed found to roughly maximize threat balancing between contaminating a large area at dangerous densities while not blowing away too quickly. The masses of chlorine considered are 4 metric tons and 16 metric tons.

The density field predicted is a 3D function of position but is evaluated at ground-level to enable fast, easy-to-interpret 2D displays such as illustrated in Figs 1.1 to 1.4. CT-Analyst can also provide time-integrated displays of the affected region that cover an extended time period. The two main time-dependent results are the contaminant 'Density' display (Fig 1.1), usually reported in mg/m^3, and the 'Health Effects' display (Fig 1.3), derived directly from the density and reported as instantaneous PAC-1, PAC-2, and PAC-3 contaminant hazard areas. When the density is measured in ppm (parts per million), the term 'Concentration' is sometimes used instead. The

Manuscript approved January 26, 2023.

integrated, extended-time displays are the 'Plume Arrival' times (Fig 1.2) of the contaminant in the region, and the contaminant 'Footprint', shown in light grey behind other source displays. The footprint is the area that may be contaminated at any time, even at very low density. The light grey area around the color-contoured cloud density in Fig 1.1 is the footprint for the 16-ton point release scenario shown.

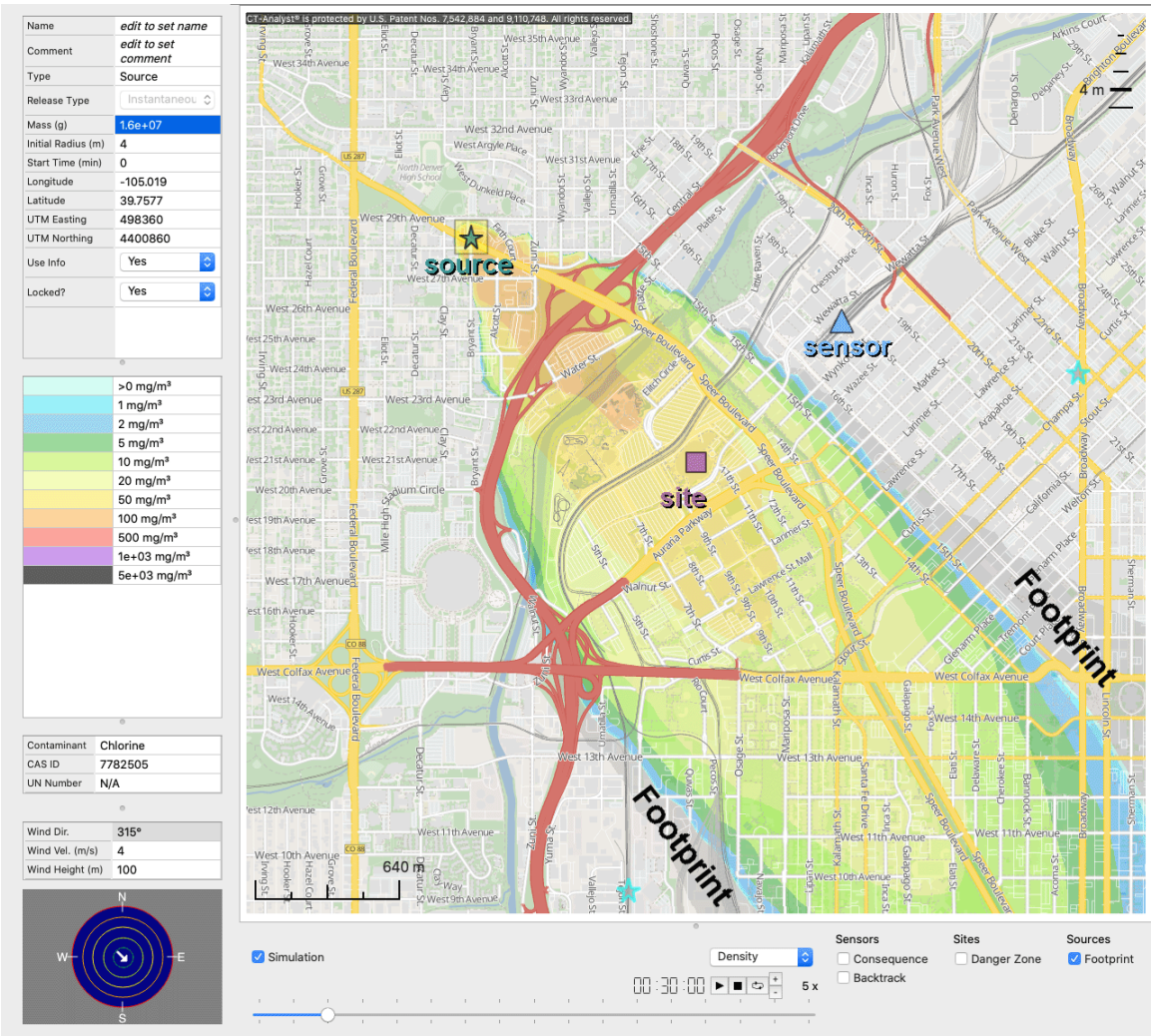

Fig 1.1 CT-Analyst interactive window and cloud density (in mg/m³) displayed 30 minutes after release of 16 metric tons of a gaseous contaminant near Denver's Ball Arena ('site'). The lidar geometry was used. The legend at the left gives the density ranges of the display colors. The light grey area surrounding the plume is the plume footprint edge, beyond which densities are zero.

Metric for Plume Comparisons: The IDA Measure of Effectiveness (MoE) is an often-used algorithm to compare one contaminant cloud dataset to another (Warner, et al., 2003; 2004; 2005). The two datasets being compared are often denoted as 'observed' and 'predicted' but the MoE can also apply to two solutions predicted by different methods or using different parameters. The MoE, based on comparing integrated areas from each dataset and their overlap area, is a snapshot at a given time that may not properly weight what has come before and may come after. There are also issues using the density to compare two cloud extents because the contaminant density can vary over many orders of magnitude from zero at a distance to thousands of parts per million right near at the source. A large, low-density area may be much

less important than a much smaller high-density region. At the very least, a density threshold must be specified to guarantee finite-size areas, as done in this report, to use the IDA Measure of Effectiveness (MoE). In practical use, as well, first responders and emergency managers cannot interpret density directly; they need to know the likely effects (symptoms) from extended exposures to the contaminant on people. Following are more examples of using the density.

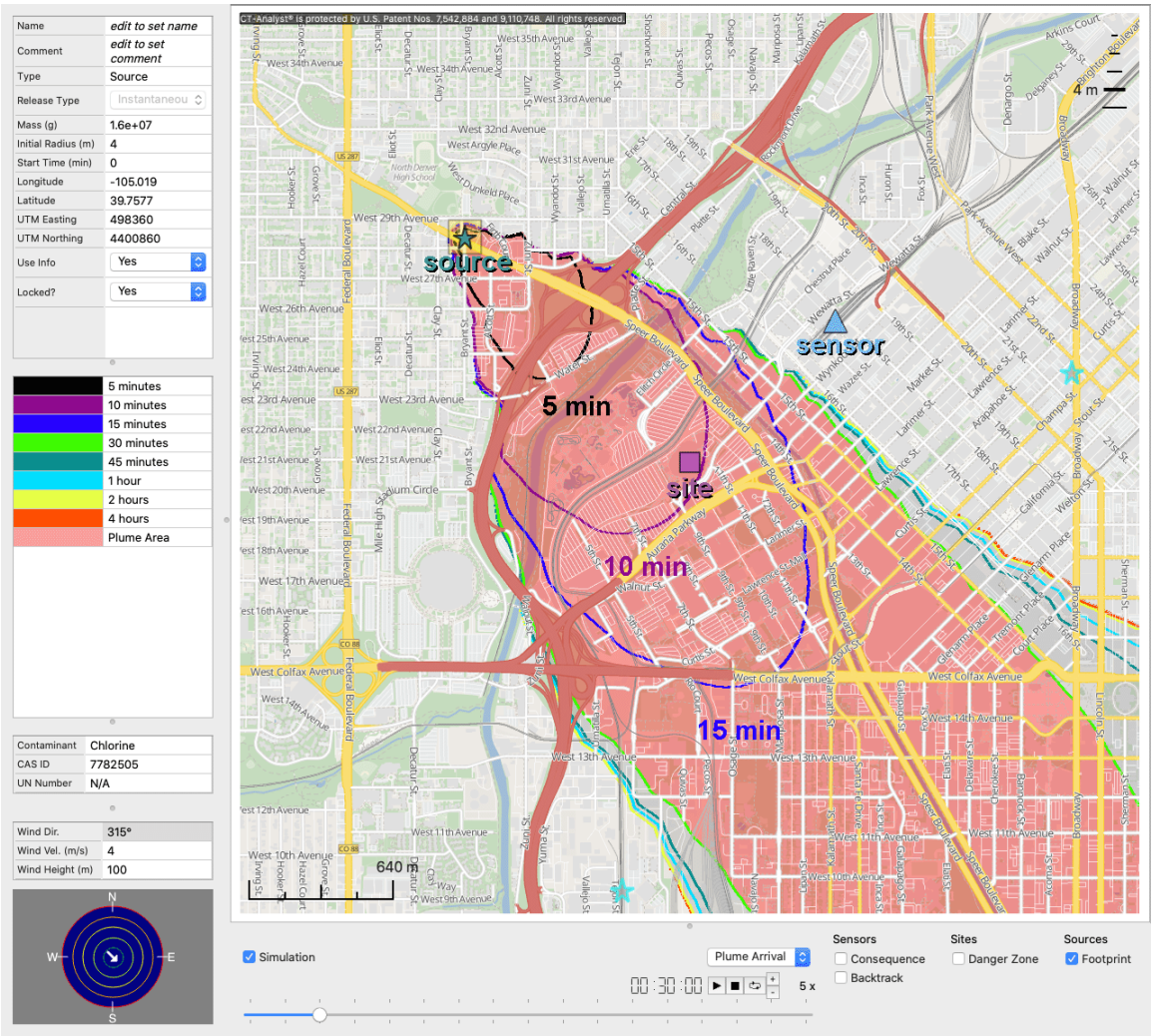

Fig 1.2 CT-Analyst interactive window and Plume Arrival display 30 minutes after release of a source at the blue-green star. The lidar geometry was used. The legend at the left gives the colors of the Plume Arrival time contours. The light grey area surrounding the plume is the plume footprint, which reaches out to the red 4-hour arrival contour.

Figure 1.2 shows CT-Analyst's 'Plume Arrival' display window for the case in Fig 1.1. The plume arrival time is the time after release, or after the start of an extended release, that the edge of the cloud first reaches each ground location. The arrival time never reaches most upwind locations when the wind direction is fixed. The arrival time is displayed as color-coded contours at a set of specific times overlaid on the cloud's current horizontal extent, which is shown in Fig 1.2 in light red at 30 minutes after release. The arrival time contours for 30 minutes and longer are near the edge of the light-grey footprint. CT-Analyst is fast enough that the predictions can be 'played' as a forward-time movie using the play-pause controls at the bottom of the window.

The Health Effects diagnostic in the release version of CT-Analyst contains a single-time evaluation of the likely effects on an exposed population. Many models, including CT-Analyst, use the PAC (Protective Action Criteria) that are defined to be the 1-hour AEGLs (EPA's Acute Exposure Guideline Levels) when the AEGL levels have been assigned. When the contaminant density exceeds the chosen PAC (AEGL) value at a specified location and time, the CT-Analyst display at that location is set to yellow (PAC-1), light red (PAC-2), or dark grey (PAC-3). The Health Effects display corresponding to Fig 1.1 using the lidar geometry is shown in Fig 1.3. In these displays the PAC-3 area is superimposed on the PAC-2 area and PAC-2 on the PAC-1 (yellow) area.

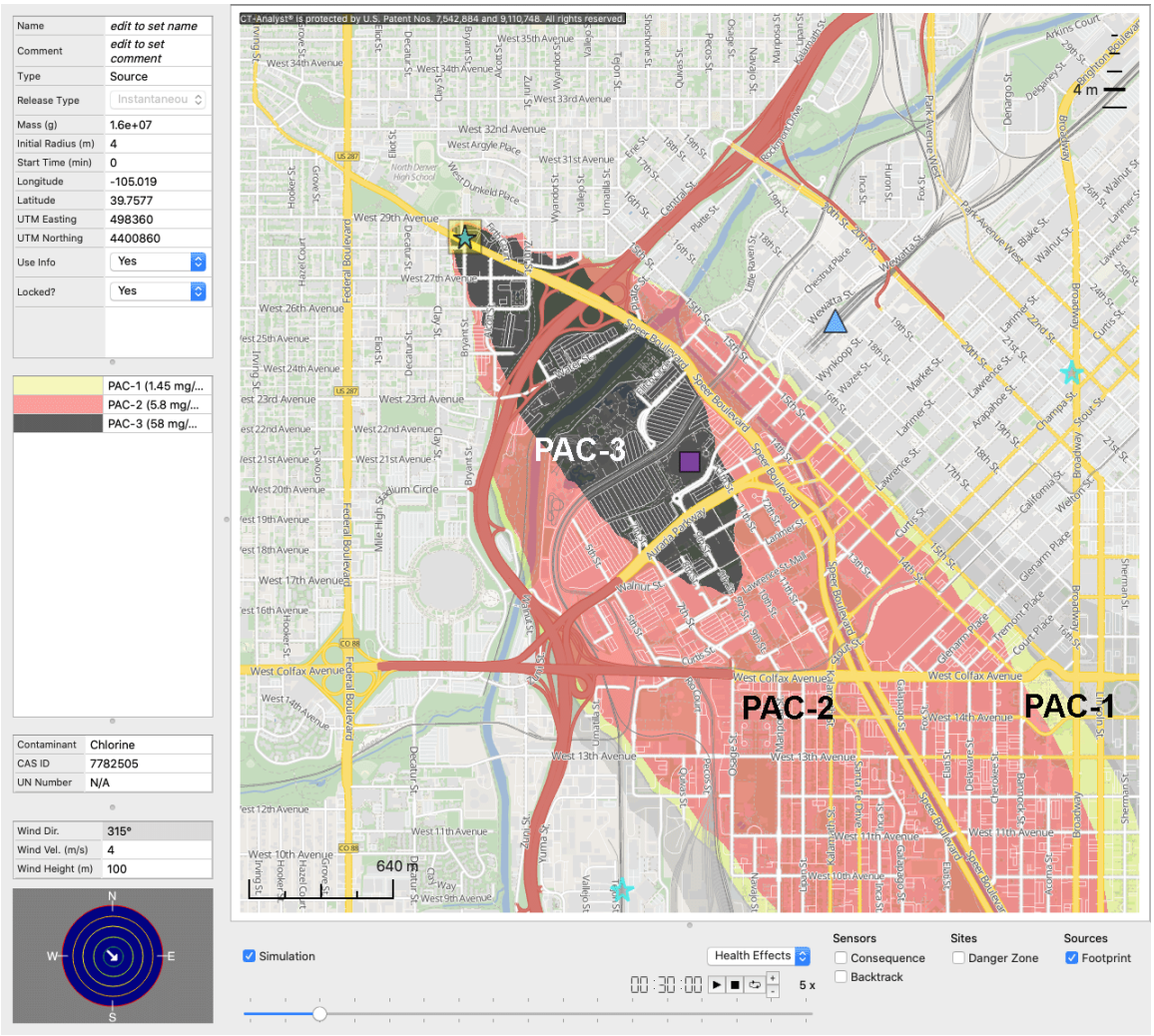

Fig 1.3 CT-Analyst interactive window and Health Effects display (PAC-3, PAC-2, PAC-1) displayed 30 minutes after release of 16 metric tons of chlorine near Denver's Ball Arena. The lidar geometry was used. The legend at the left gives the PAC density thresholds for chlorine. The light grey area surrounding the plume is again the plume footprint.

AEGL-1 is defined as the airborne concentration (expressed as ppm or mg/m^3) of a substance above which it is predicted that the general population, including susceptible individuals, could experience notable discomfort, irritation, or certain asymptomatic, non-sensory effects. AEGL-2 is the airborne concentration (ppm or mg/m^3) of a substance above which it is predicted that the general population, including susceptible individuals, could experience irreversible or other serious, long-lasting adverse health effects or an impaired ability to escape. AEGL-3 is the airborne concentration (ppm or mg/m^3) of a substance above which it is predicted that the

general population, including susceptible individuals, could experience life-threatening health effects or death. The three AEGL values are tabulated for constant density exposures lasting 10 minutes, 30 minutes, 1 hour, 4 hours and 8 hours.

For chlorine, a common toxic airborne contaminant, the 1-hour AEGL/PAC density levels are PAC-1 = 1.45 mg/m^3, PAC-2 = 5.8 mg/m^3, and PAC-3 = 58 mg/m^3. These are operationally meaningful, if somewhat flawed, thresholds for comparing the cloud's density profiles computed using different building geometry specifications. Two 3D geometries are being compared: one which we will call 'lidar' and the second which we will call 'vetted,' i.e. checked, having been assembled primarily from stereo imagery. 'LiDAR' and 'LIDAR' are also used but we will use 'lidar.' Figure 1.4 shows the equivalent CT-Analyst Health Effects display computed using the vetted Denver geometry assembled several years ago for an exercise conducted in conjunction with the Ball Arena shown at the square lavender 'site' in Figs 1.1 – 1.4.

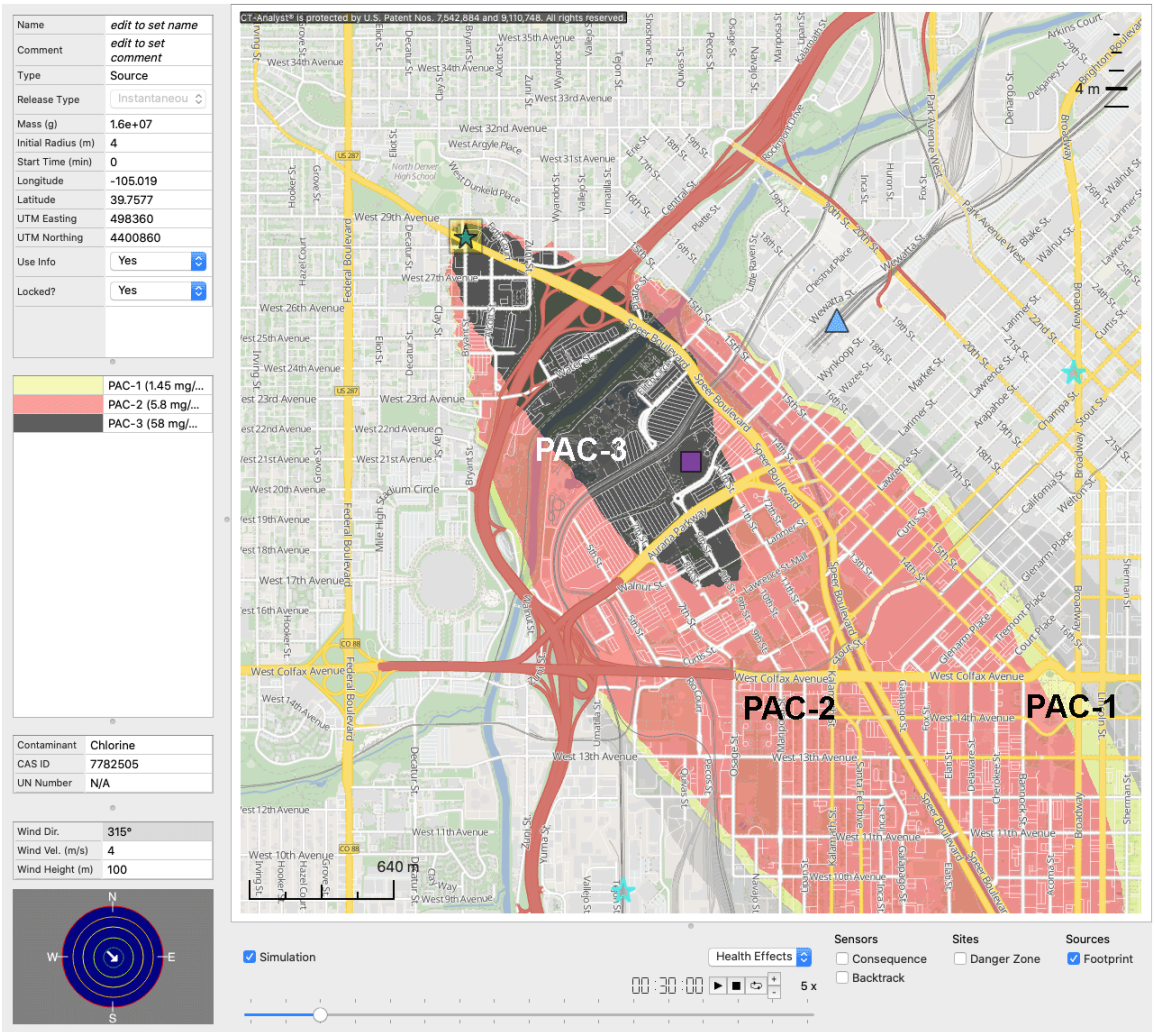

Fig 1.4 CT-Analyst Health Effects display (PAC-3, PAC-2, PAC-1) displayed 30 minutes after release of 16 metric tons of chlorine near Denver's Ball Arena. The vetted 3D Denver geometry was used. The latitude-longitude and UTM coordinates of the source are shown in the upper left legend.

Figure 1.4 shows the full CT-Analyst interactive window for the PAC Health Effects prediction 30 minutes after the instantaneous chlorine release. The differences between Fig 1.3 and Fig 1.4 are due sole to the use of the vetted database to define the 3D building geometry in 1.4. These

differences in cloud location and size are quite small, at least in this case, lending credence to using lidar geometry determinations. The cloud produced using the vetted geometry, is a little bit narrower in Fig 1.4 than the lidar-geometry result in Fig 1.3. When the cloud is narrower, the densities are higher and thus the instantaneous PAC areas extend a little farther, which is most obvious with PAC-3. The contaminated areas in this report will be defined using the density thresholds of all three PAC values. The PAC-2 areas will also include the area defined as PAC-3, and PAC-1 areas will also include both PAC-2 and PAC-3 areas.

Both Fig 1.3 (lidar geometry) and 1.4 (vetted geometry) show that all three PAC regions are nearly identical in location size and shape. 30 minutes is after the PAC-3 area has maximized, which occurs at about 22 or 23 minutes after release. As suggested, there are several issues associated with using both the area-based MoE metric and the PAC areas implemented here to evaluate the real-world impact of the differences between the geometry-defining databases.

Open-Source for Airborne Lidar Geometry: The lidar geometry is based on data from The National Map (TNM) hosted by the U.S. Geological Survey (USGS). The National Map is a collection of nationwide geographical information data. The National Map houses a collection of lidar point clouds, and topographical maps, and much more. The lidar point clouds contain points representing trees, terrain, and most important, buildings. From these, the USGS extracts the topography of the landscape, represented as a Digital Elevation Map (DEM). After specifying the geographic area, we downloaded all relevant lidar point clouds and DEMs from TNM. The point clouds were then processed using the point data abstraction library (PDAL).

PDAL is a library which provides several useful functions for point-cloud processing. Point clouds were cleaned up ('denoised') using the PDAL radius filter that deletes points not having a certain number of neighboring points within a given radius. For this research the radius was set to 2.0 meters and at least 8 neighboring points were required. Next, the process rasterized the cleaned-up point clouds using PDAL. Rasterization converts a 3D point cloud of any resolution into a heightmap, where every pixel of an image represents a height above ground. This decreases the size of the files and facilitates data processing. All rasterized data segments are stitched together into one larger file, which is then reprojected into the required size and datum/coordinate system using the Geospatial Data Abstraction Library (GDAL). We will refer to this as the lidar geometry database.

The DEMs underwent a similar process of stitching and reprojecting to become the rasterized DEM database. Next, building footprints are retrieved from the Intel building footprint database. GDAL rasterizes them and reprojects them into the proper size, hereafter the 'rasterized footprint database.' Finally, the output file is composed from the rasterized DEM and lidar databases. For every pixel of the output, if it is registered as being inside of a building, according to the rasterized footprint database, the output pixel is set to the height value recorded in the rasterized lidar database. Otherwise the pixel is set to the height of the corresponding DEM pixel. This has the effect of outputting only the terrain and the buildings. Pixels that correspond to locations that are not buildings are set to be the ambient terrain, and things that are buildings are registered in the data. This composite database is then converted to the input format accepted by FAST3D-CT, NRL's Flux-Corrected Transport, large-eddy, urban CFD model. FAST3D-CT was then used to simulate the 3D time-dependent urban wind fields based on the lidar geometry database. These 18 wind fields, each 2000 by 2000 cells wide spanning the 4 km by 4 km domain of downtown Denver Colorado, are used to produce the nomografs™ that power CT-Analyst.

Time-Dependence: Time dependence is an important factor in interpreting the results of the predictions using two slightly different geometry definitions. The differences stem not only from the intrinsic properties of the determination and processing technology but also from the dates when the geometry was determined. New buildings and buildings torn down, new walls and berms constructed for highways, and new ditches and waterways will cause differences between predictions that cannot be ascribed to the methodology used to construct the geometry dataset. These issues are always going to be important in built-up urban areas but much less so for the international scales where the IDA MoE was demonstrated. Warner, et al. (2003, 2004, 2005) applied the Measure of Effectiveness metric (MoE) to the European Tracer Experiment (ETEX) which spanned 17 countries in October 1994. Seasonal and weather effects may be important at such scales, but the addition or demise of specific buildings is almost certainly inconsequential.

Time dependence is particularly important near the beginning of an urban release where the area first affected is only a few blocks in size so local building differences near the source will be emphasized. Any significant differences in the first couple of minutes should decrease as the cloud transports through progressively larger regions where local data processing and changed geometry differences become a smaller fraction of the overall description. Toward the end of the release, time-dependence also becomes very important in regions where the density is decreasing below the threshold value chosen for the comparison. Ragged edges of the region with cloud density above threshold appear late in time and holes even begin to occur. A small, geometry-induced, percentage difference in the lateral spreading of a cloud or plume using two geometries will cause one prediction to have a lower density and thus the PAC contaminated area may actually be smaller though the plume is spreading faster.

2. Comparing Predicted Clouds from CT-Analyst's Density Display

The IDA Measure of Effectiveness (MoE) is a 2D metric for comparing predicted contaminant cloud (plume) areas to corresponding observations (see, Warner, et al., 2003, 2004, 2005). The 'observations' are generally assumed correct but the approach is symmetric so results could also be interpreted assuming the 'predictions' are correct. Here we will treat the 'vetted' geometry (VG) results for contaminant transport in downtown Denver, whatever the quantities being compared, as the more correct results while holding the newer 'lidar' geometry (LG) results as somewhat in question. At the chosen time of comparison, each location x_i, y_j in the region is analyzed to determine the level of contamination for the two urban-geometry datasets using a contamination criterion.

$C_{ij}^{LG} = .true.$ if contamination is found at location (cell) i, j using the lidar geometry.

$C_{ij}^{VG} = .true.$ if contamination is found at location (cell) i, j using the vetted geometry.

Counting all cells in the 2000 x 2000 domain where C_{ij}^{LG} is true gives N_{LG}. Counting all cells in the domain where C_{ij}^{VG} is true gives N_{VG}. Counting all cells where both C_{ij}^{VG} and C_{ij}^{LG} are true gives N_{OV}, the number of overlap cells. Clearly N_{OV} can be no larger than the smaller of N_{VG} and N_{LG}.

We define $N_{FP} = N_{LG} - N_{OV}$ as the number of false positive cells where the lidar geometry overpredicts contamination. False positive means using the lidar geometry is predicting contamination where the vetted geometry, assumed better for the sake of argument, does not.

$N_{FN} = N_{VG} - N_{OV}$ is, similarly, the number of false negatives. The terminology used, 'false negative' (FN) and 'false positive' (FP), semantically imply that the vetted geometry results are correct, or at least more correct. False Positive (FP) means a prediction of contamination where it was not observed.

Operationally, false negatives are considered bad because people might be exposed without the benefit of a warning prediction. Predictions with operational consequences must attempt, within reason, to minimize false negatives. The application of the MoE is generally applied to predictions at ground level though the definition could be expanded to treat contaminant plumes with a 3D extent above the surface. This generalization is usually ignored because density data is not readily measured high in clouds of contaminant and most people won't be exposed far above the ground. Further, the field trials in Salt Lake City showed that the contaminant density was quite homogeneous up to the average roof top heights.

The Measure of Effectiveness is defined as

$$MoE = (x, y) = \left[\frac{N_{OV}}{N_{VG}}, \frac{N_{OV}}{N_{LG}}\right] = \left[1 - \frac{N_{FN}}{N_{VG}}, 1 - \frac{N_{FP}}{N_{LG}}\right]. \qquad \text{Eq. 2.1}$$

The quantities x and y are two components of a vector in a square where (0.0, 0.0), the lower left corner, corresponds to no overlap whatsoever between the lidar-geometry cloud and the vetted-geometry cloud and (1.0, 1.0), the upper right corner, indicates full overlap (agreement) between the two results. In this report, the MoE is always (1.0,1.0) at t = 0 seconds for any comparison because the initial overlap of the two solutions is complete when the two releases originate in the same cells.

A comparison of predictions using the two geometries is shown in Fig 2.1. The left-hand column contains 15-minute snap shots of the vetted-geometry density (a), the lidar-geometry density (c), and the Measure-of-Effectiveness areas comparing the two densities (e). The right-hand column contains the 30-minute snapshots of the same quantities. The mass of chlorine released was 16 metric tons, enough so the PAC-3 exposure area would fill a significant fraction of the domain and reach the Ball Arena for at least a few minutes. The PAC-3 density threshold of 58 mg/m^3 was used for all 6 panels. Notice that the areas of all three quantities at 15 minutes are very similar to and slightly larger than the 30-minute areas. The underlying densities are being thresholded so the areas increase for a while and then eventually decreases.

The density eventually drops below the threshold value everywhere as the cloud expands so the MoE areas eventually become zero. The downwind extent of the clouds at both 15 minutes and 30 minutes are the same but the width of the clouds are qualitatively different. BY 30 minutes the clouds are shrinking because the density in the domain is decreasing. Looking downwind, the left and right edges of the potentially lethal PAC-3 area are eroding inward. An important consequence of thresholding the density to compute the MoE is that the answer changes when the mass of the released contaminant is changed because the affected area will change, even though the density is being treated linearly and could be rescaled on the fly.

In the MoE panels (e) and (f), blue is the overlap area and green is use for false positive areas where the lidar-geometry result indicates PAC-3 exposure where the vetted-geometry result does not. The red areas are where the vetted result extends beyond the lidar result and are often called 'false negative.' The color red is used to indicate a danger area where people may be exposed more seriously than the lidar-based prediction suggests. The false negative and false

positive conditions in Fig 2.1 occur in limited areas along the periphery of the blue overlap region where both geometries give the same answer.

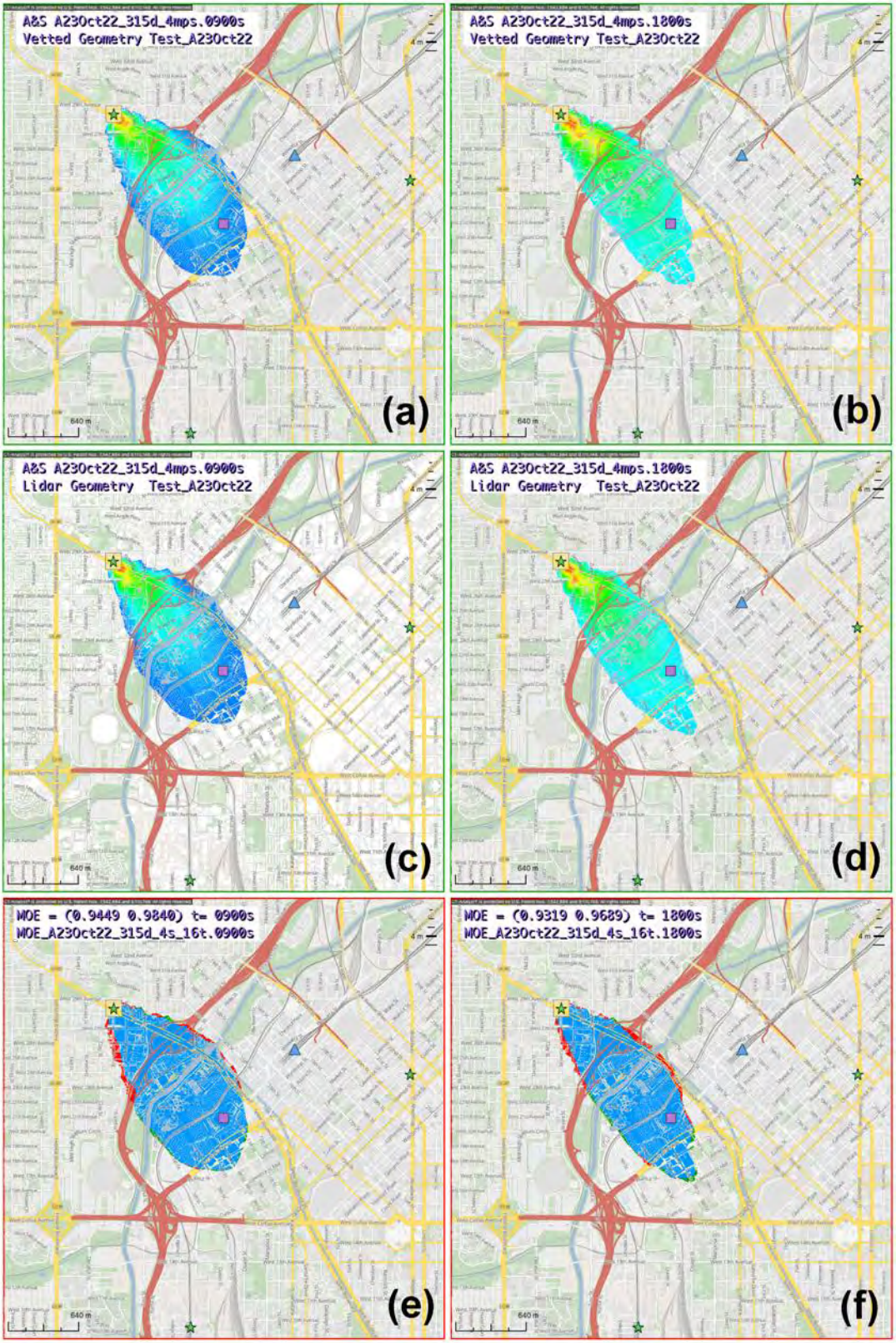

Fig 2.1 Measure of Effectiveness (MoE), (e) and (f), comparing CT-Analyst densities from the lidar-based nomograf geometry, (c) and (d), to those from the vetted geometry, (a) and (b). Results are displayed at both 15 and 30 minutes after release of 16 tons of chlorine near Denver's Ball Arena (lavender square). The density threshold in the two MoE panels is the PAC-3 value of 58 mg/m^3.

Figure 2.2 plots the individual false negative (X) and false positive (Y) components of the MoE plotted as a function of time out to 40 minutes. These two MoE components,

$$X = 1 - \frac{N_{FN}}{N_{VG}} \text{ and } Y = 1 - \frac{N_{FP}}{N_{LG}}, \qquad \text{Eqs. 2.2}$$

are first plotted separately vs time for each of the PAC cases considered. The cloud footprint from CT-Analyst is also included in Fig 2.2, plotted in green. All curves are plotted for the 4-ton release except for the PAC-3* X and Y components, which used the 16-ton release, which provides a large enough lethal area for the computation to be meaningful. Notice that no MoE_{avg} false negative (X) or false positive (Y) values are seen or plotted below about 0.87 although the definition allows values from 0.0 to 1.0. This is because the two predictions are very close.

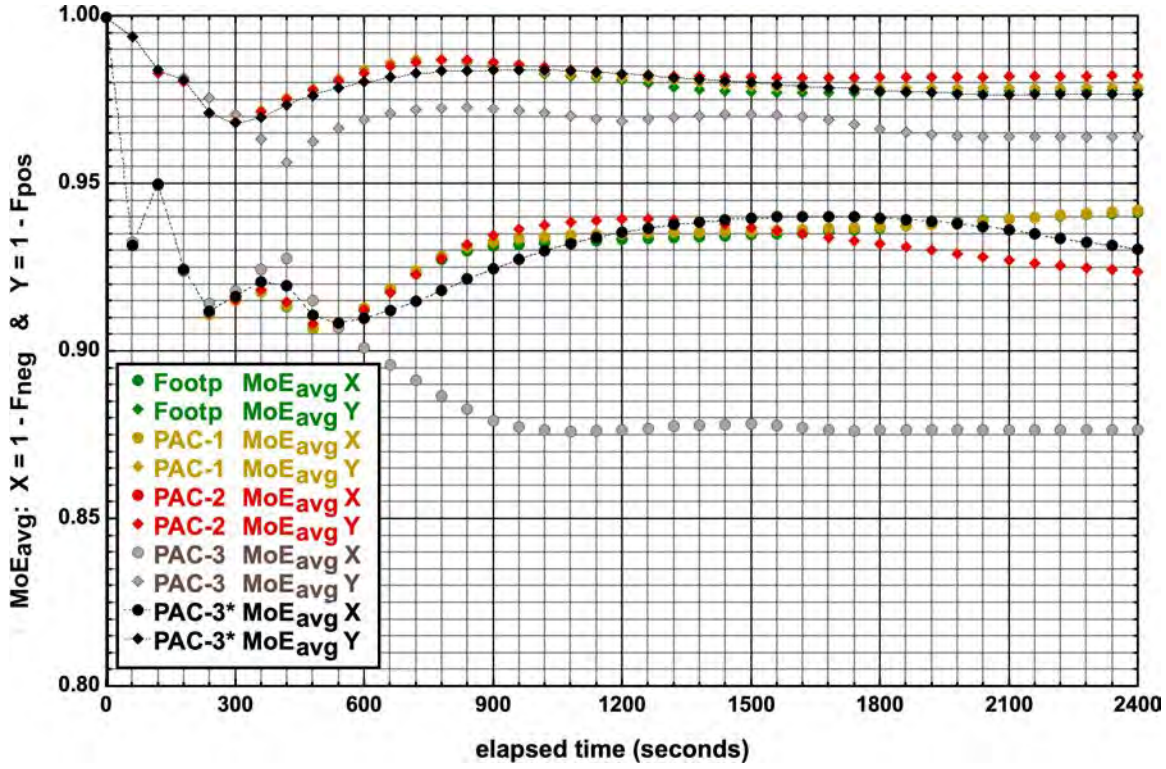

Fig 2.2 Area weighted average Measure of Effectiveness (MoE) versus time comparing CT-Analyst densities from lidar-based nomograf geometry to those from the vetted geometry after release of 4 metric tons of chlorine near Denver's Ball Arena. The density thresholds in the MoE computation are the PAC-1 to PAC-3 values of 1.42, 5.8 and 58 mg/m^3. The Footprint threshold is 0.0 density and the PAC-3* values are computed with 16 tons of chlorine.

The two solutions being compared start from the same initial conditions, as noted above, so all 10 quantities are superimposed at 1.0 in the upper left corner at t = 0 seconds. Since the MoE is defined at a specific time, rather wild fluctuations of the two MoE components X and Y occur near geometry differences close to the source. Further, severe late-time fluctuations occur as the computed PAC areas vanish at different places where the density profiles drop slightly below the chosen threshold. Both these fluctuations occur because the MoE algorithm uses

problematic threshold conditions, the 1-hour AEGLs/PACs, applied at a sequence of specific times in a rapidly changing scenario. An average over time softens both these problems. Therefore the quantities $MoE_{avg}(t)$ presented use the area weighted average of the X and Y components from t = 0 to time t. When a PAC area drops to zero, the MoE_{avg} becomes constant because the sum of the overlap areas in time and the sum of the individual components in time reach constant asymptotic values.

Figure 2.2 shows that the PAC-3 (4-ton release) and PAC-3* (16-ton release) dominate out to about 300 seconds (5 minutes) when both the PAC-2 (red) and PAC-1 (gold) areas begin to emerge from beneath the dominant PAC-3 X and Y components. The green CT-Analyst 'Footprint' X (diamonds) and Y (circles) components only appear briefly beneath the false negative PAC-1 data (gold diamonds) and the corresponding false positive data (gold circles). The $MoE_{avg}(t)$ asymptotes are seen most clearly for the light grey PAC-3 lidar curves for times close to 1800 seconds and longer. Using the lidar geometry, the PAC-3* impact area (black circles) goes to zero after 73 minutes. For the 4-ton release, the PAC-3 impact area (light grey curves) go to zero by 38 minutes, PAC-2 by 112 minutes, and PAC-1 by 210 minutes. Asymptotic times beyond 30 or 40 minutes are not shown by Fig 2.2.

A question arises in using the separate PAC areas to compute different MoEs. Should we include the PAC-3 area as part of the PAC-2 area and should we include the PAC-2 + PAC-3 area as part of the PAC-1 area. The alternative is to exclude the higher-PAC areas. In this report the PAC-1 area, for example, includes both the embedded PAC-2 and PAC-3 areas. This is really a minor concern, however, because of the shortcomings of both the instantaneous PAC area as a quantity of interest and using the MoE as a metric for comparing different datasets. We will return to these issues.

Figure 2.3 superimposes three MoE plots for 16-ton chlorine sources, marked by the star-shapes source icons. The three clouds in the figure were predicted in separate computations with the 4 m/sec wind coming from three different directions, 315^0, 75^0 and 195^0, as shown by the black arrows near sources 1, 2, and 3 respectively. The time is 600 seconds after release, during the expansion phase of the PAC-2 area but before the areas covered by the three clouds would overlap. The influence of the local geometry is clear from the different cloud shapes and sizes. Again, blue marks the overlap areas for the three MoE computations, red marks lidar false negative areas, and green marks lidar false positive areas.

In the figure lidar false negative areas seem to outweigh the false positive areas by a factor of two or three at 10 minutes but the differences from the ideal result 1.0 are all less than 10% in these three cases. The area weighted MoE_{avg} components all vary significantly as a function of time as shown in Fig 2.4. These X and Y variations are described above with respect to Fig 2.2 and are quite similar here. We need to note that is not clear which of the two geometry results are actually more accurate. In fact this judgement probably varies from place to place in the 4 km by 4 km downtown region being treated. Some buildings in the vetted geometry may be missing from the lidar dataset and vice versa. Some rooftops in the vetted geometry may be flattened or truncated and there are errors at edges and corners with lidar despite the regularization caused by truncating the lidar geometry heights to lie within the Intel building footprint database.

It is also worth noting that the plume envelopes computed with the two somewhat different geometries are noticeably diverted toward the river basin direction for sources 2 and 3 which are

computed with wind directions, 75^0 and 195^0, that have a significant component along the river. Further, while there are some areas of 'false negative' and 'false positive' comparison, both components of the two-dimensional MoE are well over 90%, and the six values average over 0.94.

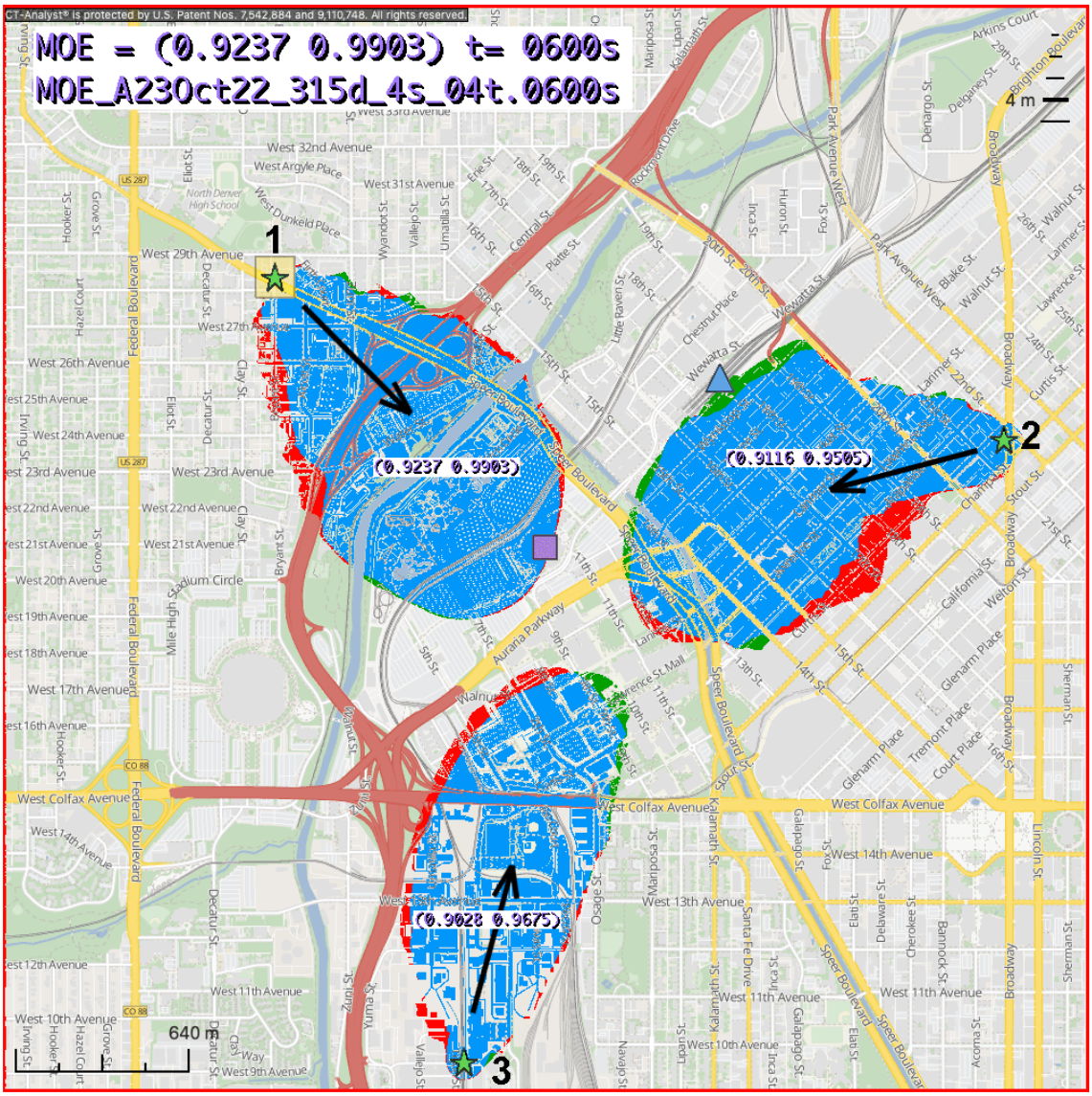

Fig 2.3 Instantaneous Measure of Effectiveness (MoE) 10 minutes after release of 16 metric tons of chlorine near Denver's Ball Arena, comparing CT-Analyst densities from lidar nomograf geometry to those from vetted geometry. The density threshold in the MoE computation is the PAC-2 value of 5.8 mg/m^3. The computed MoE components are shown in the superimposed white rectangles.

Figure 2.4 plots the time dependent MoE_{avg} X and Y components, as in Fig 2.2 above, for PAC-2 (4 tons of chlorine) and PAC-3* (16 tons) as a function of time for the three sources and their corresponding wind directions shown in Fig 2.3. X-components (circles) indicate lidar false negatives and Y-components (diamonds) indicate lidar false positives. Shades of black and grey indicate potentially lethal PAC-3 results and Shades of red indicate serious PAC-2 symptom conditions.

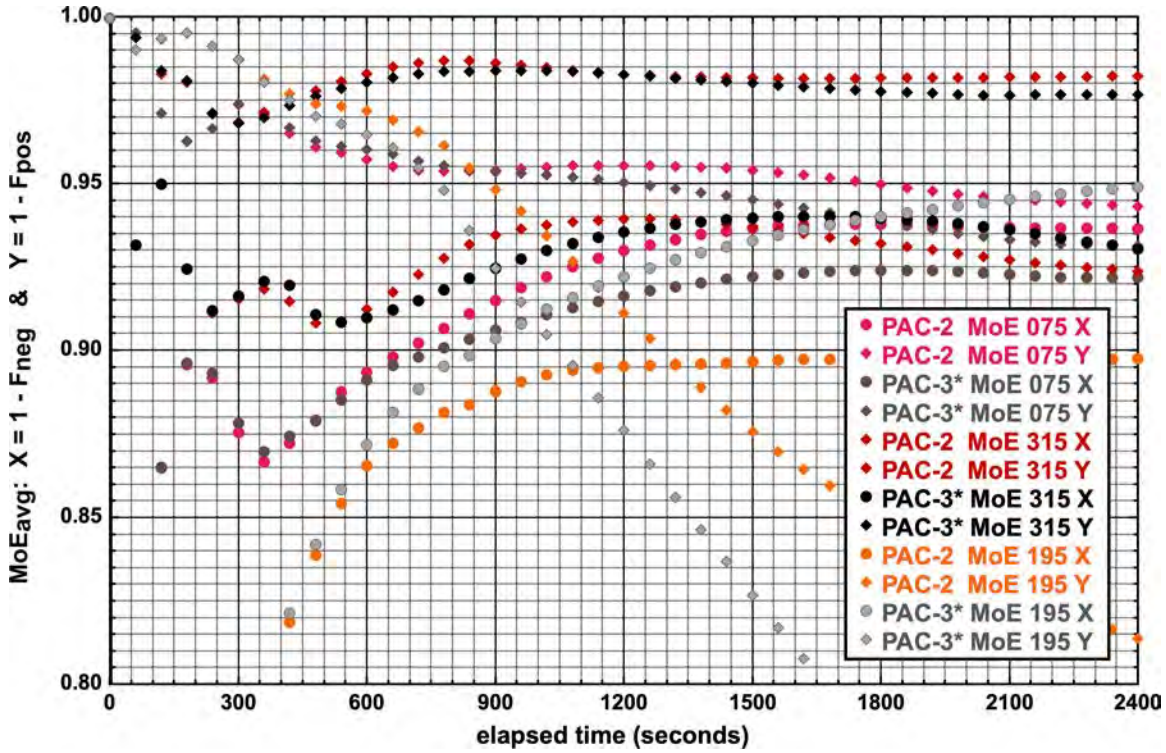

Fig 2.4 Area weighted average Measure of Effectiveness (MoE_{avg}) versus time comparing CT-Analyst densities from lidar-based nomograf geometry to those from the vetted geometry after a release of chlorine near Denver's Ball Arena. The density thresholds in the MoE_{avg} computation are the PAC-2 and PAC-3 values of 5.8 and 58 mg/m³. The PAC-3* data were computed with 16 tons of chlorine.

The area-weighted MoE_{avg} curves in Fig 2.4 eventually approach an asymptotic value as time increases. These limiting values are reached when the late-time density has dropped below the PAC threshold value everywhere. These asymptotes are generally at 0.90 or above. i.e., less than 10% difference between the results from the two geometries. The figure only extends to 40 minutes, however, so a few of these components are still changing and thus the MoE_{avg} values are changing (decreasing). Two of the curves, the grey and light red diamonds of the 195^0 Y components in the lower right of the figure, do not seem to be reaching an asymptote. This is because the plot's vertical axis only extends from MoE_{avg} = 0.8 to 1.0; smaller MoE_{avg} values are not plotted. The runs actually continued out to an hour where the PAC-3* Y (grey diamonds) is flattening off at about 0.6 and the PAC-2 Y component (light red diamonds) is flattening off a about 0.75.

Figures 2.2 and 2.4 are not the usual way to display MoE values. Rather, an X-Y 2D plot is usually used, as shown in Fig 2.5, which recasts the data of Fig 2.4. All 6 curves begin at (1.0, 1.0) in the upper right corner. There are strong but brief excursions, in the first minute or two, of the 195^0 PAC-2 and PAC-3* X components to 0.59 off the upper left of the figure. Fig 2.5 is restricted to the range 0.7 to 1.0 in both X and Y to expand the region where most of the points are, 0.85 to 1.0 in both X and Y. At early times the clouds are small so local geometry differences involving a few building representations near the source have an exaggerated effect on the MoE_{avg} values.

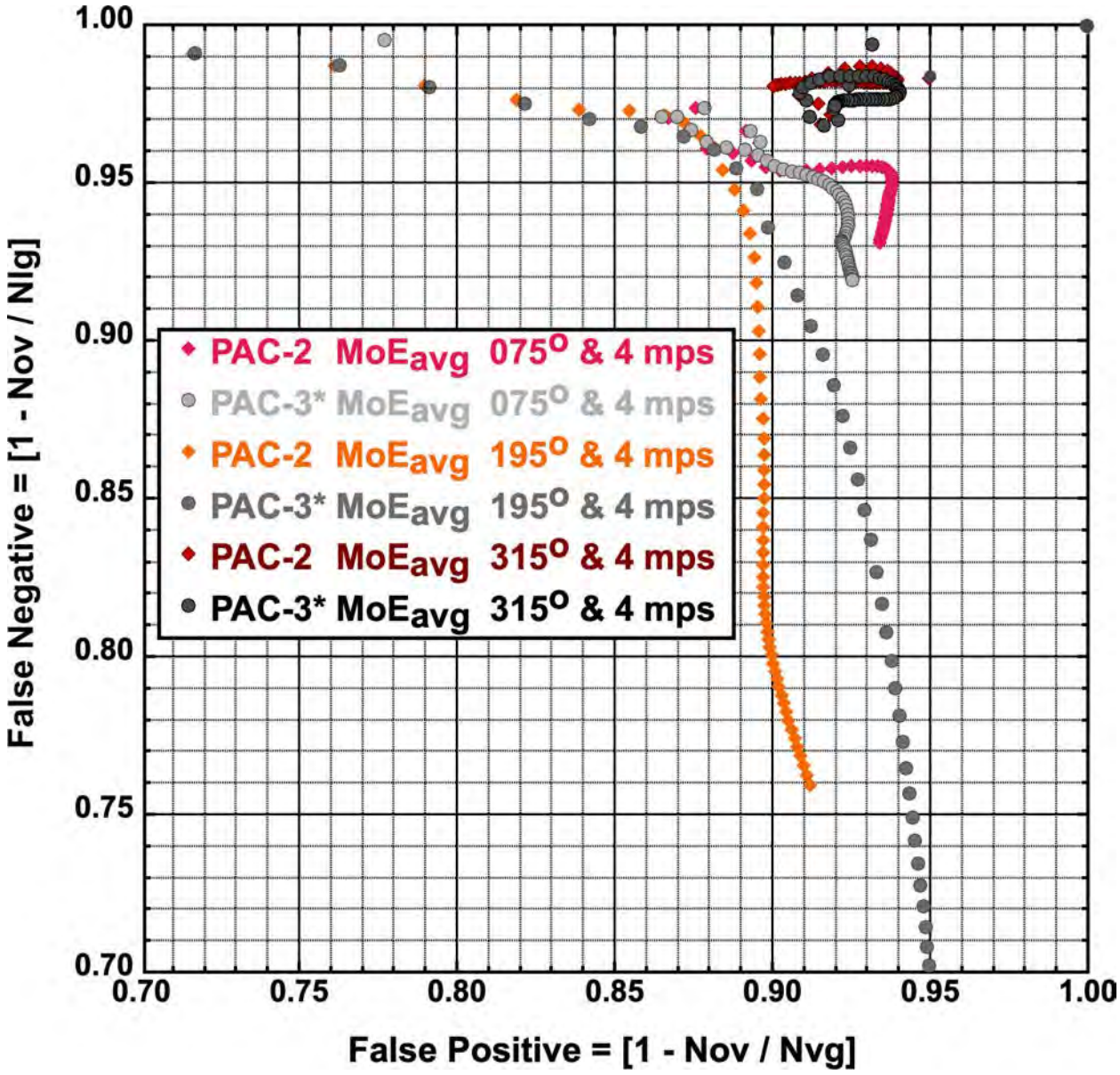

Fig 2.5 MoE_{avg} X-Y plot comparing CT-Analyst densities from lidar-based nomograf geometry to those from the vetted geometry after a chlorine release near Denver's Ball Arena (lavender square). The density threshold in the MoE is the PAC-3 value of 58 mg/m^3. The two 195^0 cases have PAC impact areas that are nonzero and still decreasing when these runs ended at 60 minutes.

The issues with the rapidly changing time dependence near the source, the decrease of the density values below PAC threshold densities late in time, and the use of areas as the metric of comparison will be discussed briefly in Section 3 but will be addressed more carefully in planned future work.

3. Conclusions and Discussion

Figures and discussion above give good, if preliminary, evidence that the 3D buildings and terrain from lidar-acquired geometry and the existing vetted geometry, generally based on stereo imagery, give very similar results seen through the lens of the CT-Analyst® density and health effects predictions. Figures 1.3 and 1.4 showed CT-Analyst window screenshots of the Health Effects display 30 minutes after release. The location, size and shape of the PAC-1, 2, and 3 exposure regions at 30 minutes there are remarkably similar.

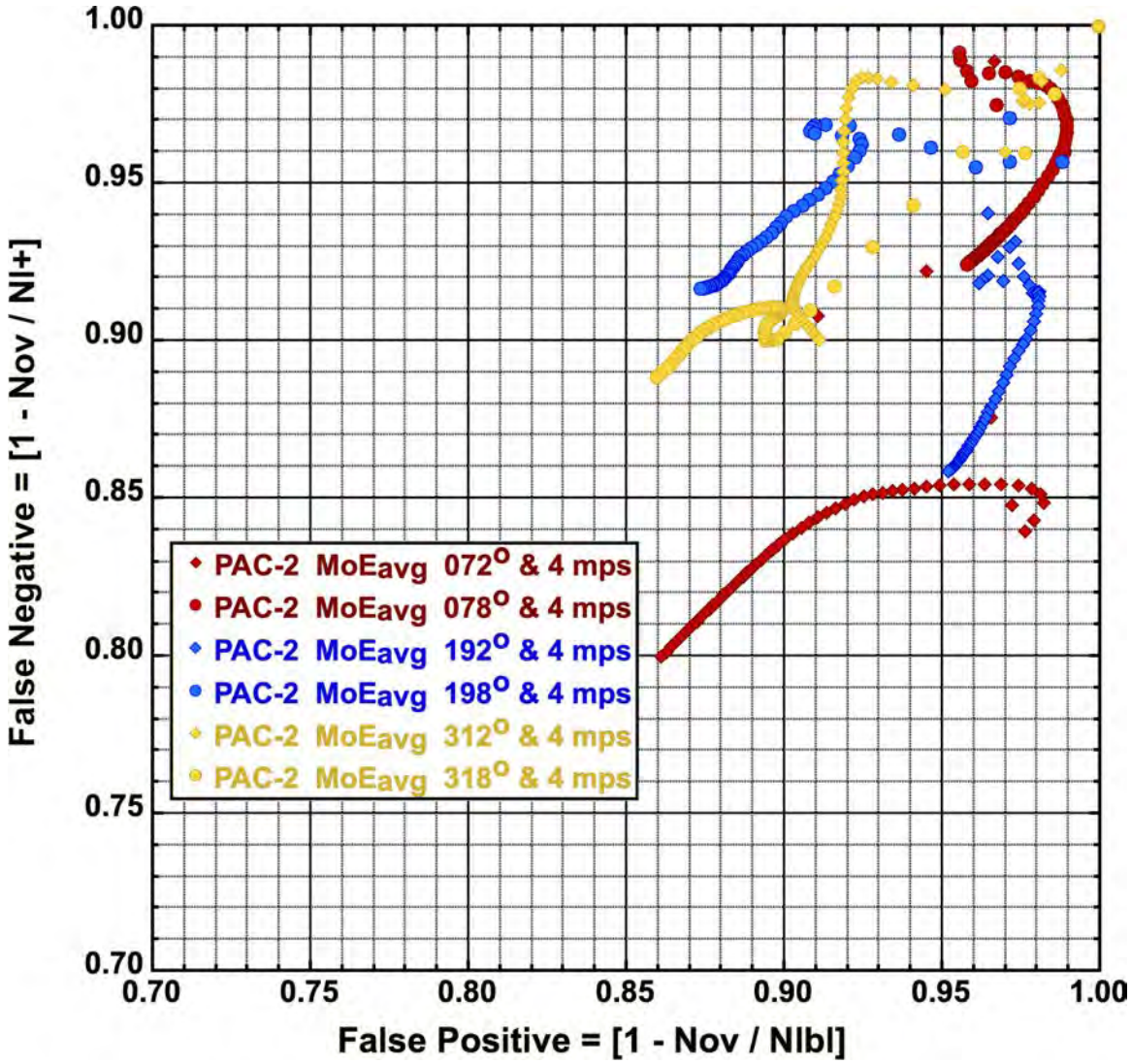

Fig 3.1 MoE_{avg} comparing CT-Analyst densities from lidar-based nomograf geometry to those from the vetted geometry after a chlorine release near Denver's Ball Arena (lavender square). displayed 20 minutes after. The density threshold in the MoE is the PAC-3 value of 58 mg/m^3.

Figures 2.1 and 2.3 provide additional evidence, if only semi-quantitative, with visual examples of the close comparison obtained including Measure of Effectiveness (MoE) metric evaluations at 10, 15 and 30 minutes after the chlorine release and including data from three source locations with three different prevailing wind angles above the urban landscape. The final Fig 3.1 provides another plot showing that the results using the two geometries are close using more data from the three source scenarios introduced for Fig 2.5. The intent is to show that the

MoE_{avg} differences between the results from the two geometries using a single scenario is comparable to the differences found by comparing clouds using only a single urban geometry but with prevailing winds from two slightly different wind angles. Using CT-Analyst and the lidar geometry, time-dependent density fields at one-minute intervals were made with winds displaced by $+3^0$ and -3^0 degrees from the 315^0, 75^0, and 195^0 wind angles used with the three sources in Fig 2.5. The results of these 6 $MoE_{avg}(t)$ runs are plotted in Fig 3.1 above.

Most of the data points are in the upper-right quadrant of the figure, as also is the case with the data in Fig 2.5. In the situations of Fig 3.1, however, the large initial excursions of X and Y in the first two or three minutes of Fig 2.5 are absent because, using the same geometry, there are no building-geometry differences near the three sources. The late-time relaxations are also more limited because the cloud-spreading characteristics of the single lidar geometry are only minimally different between nearby wind angles. Comparing these two figures suggests that the practical differences between the lidar and the vetted stereo imagery geometry definitions cause about the same deviations as two- or three-degree errors in determining the prevailing wind direction. Since the actual prevailing wind direction is one of the most uncertain inputs in using CT-Analyst, or any other contaminant prediction tool, in a real incident, the operational impact of the geometry differences can be viewed as problematic.

Converting these clear indications of the usefulness of the lidar-based geometry to solid quantitative evidence is work for the future. The issues were discussed earlier, the use of relative areas as the metric without an underlying physical argument and the use of an instantaneous time snapshot to characterize an extended-duration, time-dependent phenomenon. In this report the PAC conditions were introduced to set a rationale for choosing the necessary density threshold for evaluating the MoE. Extending this approach to an area weighted time average of the MoE reduces some of the difficult associated with early times and late times. However, it should be possible to do considerably better. The comparisons will be extended to more source locations, a number of prevailing wind angles, and a more meaningful definition of the operational health effects.

In the future we plan to remove the dependence on the source release mass, leading to the differences between the PAC-3 (4 ton scenario) and PAC-3* (16 ton scenario) to keep the total PAC-2 and PAC-3 impact areas within the complex-geometry domain. We plan to use time-independent quantities that do not involve the instantaneous PAC conditions for scenarios that will replace the MoE or the area-weighted average MoE with a quantity that should be of direct interest to emergency managers and first responders. We will identify the locations in the region where the release could cause symptoms at each of the three levels and determine when the exposure at that level will be over. This time-independent result can later be generalized to an integration of the toxic load accumulated by exposed individuals at each location, using a density dependent generalization of the table of AEGL conditions (Boris and Patnaik, 2014). This will remove the dependence of the health effects computations on the largely irrelevant 1-hour AEGLs. This proposed metric should be called the Symptom Onset time. It tells when each of the three symptom conditions is reached, or not reached, every place in the domain.

Acknowledgements:

We wish to acknowledge the advice, help, and suggestions of colleagues who have worked with us in developing and implementing CT-Analyst - Bernd Leitl, Susanne Fischer, Frank Harms, Denise Herwig, Hannibal Fossum, Mi-Young Obenschain, Anders Helgeland, Teresa Lustig and David Lamensdorf. We also wish to acknowledge the NRL base program for its steadfast support in performing the research which has led to the developments discussed here.

References:

Steve Warner, Nathan Platt, and James F. Heagy, 2003, "Application of User-Oriented MoE to Transport and Dispersion Model Predictions of the European Tracer Experiment," Institute for Defense Analyses (IDA) Paper P-3829, November 2003.

Steve Warner, Nathan Platt, James F. Heagy, 2004, "Application of user-oriented measure of effectiveness to transport and dispersion model predictions of the European tracer experiment," *Atmospheric Environment* **38**, pp 6789–6801, 2004.

Steve Warner, Nathan Platt, and James F. Heagy, 2005, "Comparisons of transport and dispersion model predictions of the European tracer experiment: area- and population-based user-oriented measures of effectiveness," *Atmospheric Environment* **39,** pp 4425–4437, 2005.

J. Boris, G. Patnaik, K. Obenschain, A. Moses, M-Y. Obenschain, T.R. Young, Jr, J. Delaney, and J. Donnelly, 2010, "Fast and accurate prediction of windborne contaminant plumes for civil defense in cities," The Fifth International Symposium on Computational Wind Engineering (CWE2010), Chapel Hill, North Carolina, USA, 23-27 May 2010.

B. Leitl, F. Harms, E. Berbekar, J. Boris, G.Patnaik, K. Obenschain, and S. Fischer, 2016, "Local-Scale Hazmat Dispersion Modeling for First Responders Based on High-Resolution Computational Fluid Dynamics - an Overview of CT-Analyst Hamburg," *Chemical Engineering Transactions* **48**, June 2016, ISBN 978-88-95608-39-6, ISSN 2283-9216.

B. Leitl, K. Storm, S. Fischer, F. Harms, J. Boris and G. Patnaik, 2017, "On the simulation of wind-driven hazardous material dispersion in complex built-up terrain - Potential and drawbacks of dispersion modeling," *Zeitschrift für Forschung und Technik im Brandschutz vfdb* **66** (3), pp 151–158, August 2017.

G. Patnaik, J. Boris, D. Hertwig, B. Leitl, F. Harms, S. Fischer and K. Storm, 2017, "Reduced-Order Model for Urban Transport," Chemical and Biological Defense Science & Technology Conference, Long Beach CA, 28030, Nov 2017.

K. Obenschain, J. Boris, and G. Patnaik, 2004, "Using CT-Analyst to Optimize Sensor Placement," SPIE D&S Symposium, Paper 5416-2, Proceedings of the SPIE, Chemical and Biological Sensing V, pp 14–20, Patrick Gardner (ed), (SPIE, Bellingham WA, 2004).

J. Boris and G. Patnaik, 2014, "Acute Exposure Guideline Levels (AEGLs) for Time Varying Toxic Plumes," NRL Memorandum Report NRL/MR/6003–14-9493, 2014.

J. Boris, G. Patnaik, K. Obenschain, 2019, "Health-Effect Hazard Areas for Airborne Contaminant Agents," NRL Memorandum Report MR/6003–19-9843, 15 January 2019.

Early CT-Analyst References (not otherwise referenced in the text):

J. P. Boris, K. Obenschain, T. R. Young, G. Patnaik, and R. Scott, 2001, "CT-Analyst: Software for Zero Latency, High Fidelity Emergency Assessment of Airborne Chemical, Biological, and Radiological (CBR) Threats," HPC User's Conference (2001), Navy Patent Case Number 84,431 (2003).

J.P. Boris, K. Obenschain, G. Patnaik and T. Young, Jr., 2002, "CT-Analyst: Fast and Accurate CBR Emergency Assessment," Proceedings, First Joint Conference on Battle Management for Nuclear, Chemical, Biological and Radiological Defense, Williamsburg VA, 4–8 November 2002.

Julie Pullen, Jay Boris, Theodore Young, Gopal Patnaik and John Iselin, 2003, "Comparison Studies of Plume Morphology using a Puff Model and an Urban High-Resolution Model," CD Proceedings: 7th Annual GMU Transport and Dispersion Modeling Workshop, George Mason University, Fairfax VA, 17 June 2003.

Gopal Patnaik, Jay P. Boris, Fernando F. Grinstein and John P. Iselin, 2003, "Large Scale Urban Simulations with the MILES Approach," AIAA Paper 2003-4104, 16th AIAA CFD Conference, Orlando FL, 25 June 2003, (AIAA, Reston VA, 2003).

Jay Boris, Jack Fulton, Keith Obenschain, Gopal Patnaik and Theodore Young, Jr., 2004, "CT-ANALYST: Fast and Accurate CBR Emergency Assessment System," SPIE D&S Symposium, Paper 5416-1, SPIE Proceedings: **Chemical and Biological Sensing V**, pp 1–13, Patrick Gardner (ed), (SPIE, Bellingham WA, 2004).

Keith Obenschain, Jay Boris and Gopal Patnaik, 2004, "Using CT-Analyst to Optimize Sensor Placement, SPIE D&S Symposium, Paper 5416-2, SPIE Proceedings: **Chemical and Biological Sensing V,** pp 14–20, Patrick Gardner (ed), (SPIE, Bellingham WA, 2004).

T. R. Young, J. P. Boris, S. Cheatham, J. Fulton, C. Lind, K. Obenschain, G. Patnaik, 2004, "CT-Analyst: Fast and Accurate CBR Emergency Assessment," Proceedings: 13th Conference on the Applications of Air Pollution Meterology, Paper J5.5, August 2004.

Jay Boris, Sally Cheatham, Gopal Patnaik, Michael McGinnis, Keith Obenschain, Theodore Young, Jr., and Tom Rappolt, 2004, "Variability, Validation, and CFD: There is No Truth!," Proceedings: 8th Annual GMU Transport and Dispersion Modeling Workshop, George Mason University, Fairfax VA, 14 July 2004.

T. Young, Jr., J. Boris, S. Hooper, C. Lind, K. Obenschain, and G. Patnaik, 2004, "Emergency Assessment With Sensors And Buildings: Advances In CT-Analyst Technology," Proceedings: CBIS 2004, Williamsburg VA, 19–21 October 2004.

G. Patnaik, K. Obenschain, and J. Boris, 2006, "System and Method for Zero Assessment of Airborne Chemical, Biological and Radiological Threats by Optimizing Sensor Placement," Navy Patent Case 97,281 (2006)